The Reduction Behavior of Cubic In_2O_3 Nanoparticles by Combined Multi-*In Situ* Spectroscopy and DFT

Marc Ziemba[1], Leon Schumacher[1], Christian Hess[1*]

[1]Eduard Zintl Institute of Inorganic and Physical Chemistry, Technical University of Darmstadt, Alarich-Weiss-Str. 8, 64287 Darmstadt, Germany

*email: christian.hess@tu-darmstadt.de

Keywords

In_2O_3, oxygen vacancies, Raman spectroscopy, DFT, resonance effects, UV-Vis spectroscopy, XPS

Graphical Abstract

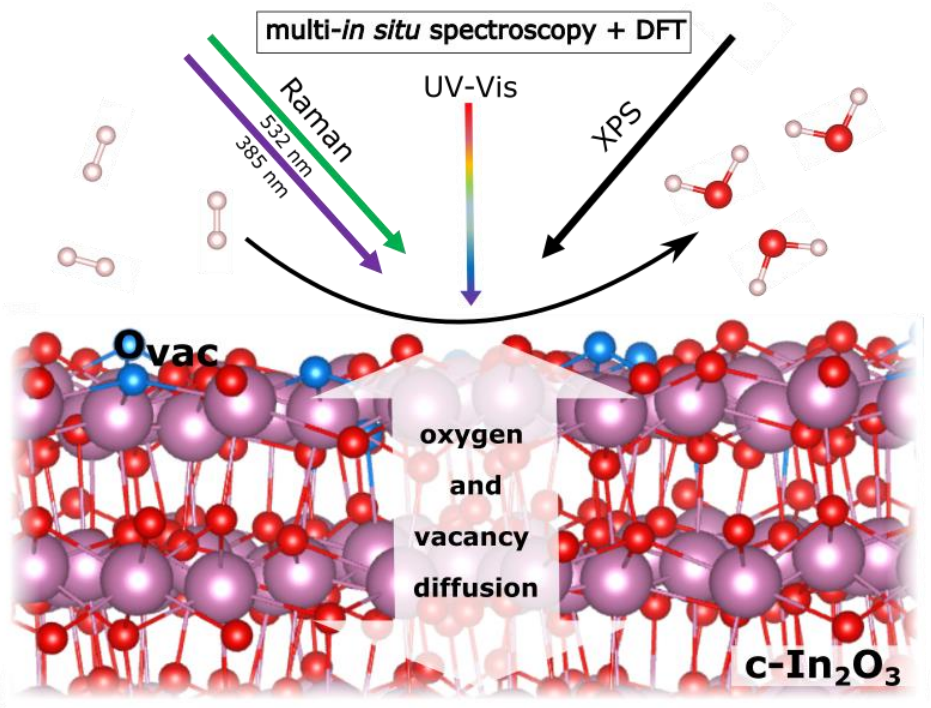

Abstract

Indium oxide (In_2O_3) has emerged as a highly active catalyst for methanol synthesis by CO_2 hydrogenation. In this work we elucidate the reduction behavior and oxygen dynamics of cubic In_2O_3 nanoparticles by *in situ* Raman and UV-Vis spectra in combination with density functional theory (DFT) calculations. We demonstrate that application of UV and visible Raman spectroscopy enables, first, a complete description of the In_2O_3 vibrational structure fully consistent with theory, and second, the first theoretical identification of the nature of defect-related bands in reduced In_2O_3. Combining these findings with quasi *in situ* XPS and *in situ* UV-Vis measurements allows the temperature-dependent structural dynamics of In_2O_3 to be unraveled. While the surface of a particle is not in equilibrium with its bulk at room temperature, oxygen exchange between the bulk and the surface occurs at elevated temperatures, leading to an oxidation of the surface and an increase in oxygen defects in the bulk. Our results demonstrate the potential of combining different *in situ* spectroscopic methods with DFT to elucidate the complex redox behavior of In_2O_3 nanoparticles.

Cubic indium oxide (In_2O_3, $Ia\bar{3}$) shows high catalytic activity for a variety of reactions, such as CO_2 hydrogenation to methanol or the reverse water–gas shift reaction.[1–6] To gain insight into the mode of operation of In_2O_3 catalysts, a detailed understanding of their redox behavior, including the associated oxygen dynamics and the In_2O_3 defect structure, will be required. In this context, oxygen vacancies could be identified as active sites during methanol synthesis or the reverse water gas shift reaction, since CO_2 is activated over In_2O_{3-x} sites formed by H_2.[2,7–9] Furthermore, selective hydrogen combustion by In_2O_3 has recently been shown to be an essential part of tandem catalysts for propane to propylene conversion.[10] Since both processes involve oxygen vacancies, there is a need for a detailed understanding of their formation and dynamics. In this context, previous studies have shown that at elevated temperatures (300 °C) and under reducing conditions metallic indium is formed and defect-related Raman bands occur.[11,12] However, the nature of these bands and the interplay of surface and sub-surface/bulk processes, which is of great importance for catalysis, is still not clarified, despite previous work on the vibrational analysis of In_2O_3.[13–19]

In this study, we investigate catalytically interesting In_2O_3 nanoparticles with respect to their structural behavior under oxidative and reductive conditions, both experimentally and theoretically. By using multi-wavelength *in situ* Raman spectroscopy and, in particular, selective resonance enhancement at 385 nm excitation, a profound description of In_2O_3-related vibrational modes is provided. Furthermore, we explore the oxygen dynamics at the surface and in the bulk, using a combination of UV-Vis and X-ray photoelectron (XP) spectroscopy, as well as X-ray diffraction (XRD).

After synthesis by precipitation of indium(III) nitrate hydrate, the In_2O_3 particles were first characterized by N_2 adsorption at 77 K, XRD, transmission electron microscopy (TEM), and XPS (for details see SI). Using N_2 adsorption and the Brunauer–Emmett–Teller (BET) model, the specific surface area was determined as 39 m^2/g (for isotherms see Figure S1). The XRD results show that only cubic ($Ia\bar{3}$) In_2O_3 is present (see Figure S2) and, by means of the

Scherrer equation, the size of the particles was calculated to be 19 nm. These results are consistent with the TEM images (see Figure S3), which additionally show that the particles are present as sheets terminating with a In_2O_3(222) surface, based on the observed distances between the lattice planes of 0.29 nm.[20] XPS analysis reveals an O:In ratio of 1.47 (see Table S1; see SI for details on the calculation), indicating that oxygen defects are already present in the as-prepared state. However, it should be noted that detailed analysis of the C 1s photoemission reveals a shoulder at higher binding energies (~ 289 eV), indicating the presence of oxygen containing adsorbates, e.g., carbonates (see Figure S4),[21] which increase the O:In ratio. We can therefore conclude that there are significantly more defects present on the surface than *ex situ* XPS reveals.

In the following, we will first discuss the results from multi-wavelength Raman spectroscopy. Figure 1A shows *in situ* Raman spectra of In_2O_3 at 532 nm laser excitation. Under O_2/Ar flow the Raman spectra are characterized by four strong bands at 307, 366, 496, and 629 cm^{-1}, which can readily be assigned to $\delta(InO_6)$, $\nu(InO_6)$, In-O-In, and $\nu(InO_6)$ vibrations of cubic In_2O_3, in accordance with the literature.[16,22] Comparison of the temperature-dependent O_2/Ar spectra (black and green) reveals a red shift and a change in full width at half maximum (FWHM) at 120 °C, which originate from a temperature effect, as the spectra of reduced In_2O_3 (blue) show the same positions. In summary, it can be said that a low degree of reduction has no influence on the Raman positions, just the temperature does, since at 120 °C the spectra in O_2/Ar and H_2/Ar show the same positions. After oxygen treatment at 25 °C, hydrogen was passed over the sample at 25 °C, but did not lead to detectable changes in the Raman spectrum. In contrast, at 120 °C in H_2/Ar flow, the overall intensity decreased and the phonon ratios changed significantly. Furthermore, new Raman features appeared at 254, 413, 555, and 589 cm^{-1}; the broad band at 413 cm^{-1} had already been observed in earlier studies but its exact nature has not been clarified yet.[11] As part of this study, measurements were also performed at 250 °C, but under these conditions Raman spectra are hampered by increased absorption (see

Figure 3) and fluorescence and are therefore not shown. For this reason, the sample was subsequently cooled to 25 °C under argon and another spectrum was recorded (see Figure S6). Again, the spectrum is dominated by the increased absorption (see yellow spectrum in Figure 3A), but the In_2O_3 phonons are visible, however defect-related features remain hidden by the higher background. A significant feature of the band positions is that they exhibit a red shift in contrast to the spectra at 120 °C under H_2. This highlights the fact that the bands shift red at higher defect concentrations. In addition, we see bands at 1499 cm^{-1} and 1554 cm^{-1} (see Figure S7), which may be attributed to In-H vibrations.[23–26] The intensity ratio of these bands changes with the gas-phase composition, i.e., the band at 1499 cm^{-1} increases upon exposure to hydrogen, indicating the activation of H_2. The chemical environment appears to have a strong influence on the band position, as for example In-H species on CHA zeolites have been shown to exhibit bands within 1700–1800 cm^{-1}.[27] In contrast, OH-related Raman bands shows only temperature-related changes and completely disappear upon treatment at 250 °C in H_2 flow (see Figure S8).

As an additional laser wavelength for Raman spectroscopy, we used 385 nm excitation, which minimizes fluorescence and, due to an electronic resonance with In_2O_3, enables selective resonance enhancement of In_2O_3-related modes. A comparison of the two excitation wavelengths shows (see Figure 1B) that the 385 nm Raman spectrum reveals additional phonons, which were not detectable or only very difficult to detect with 532 nm excitation.

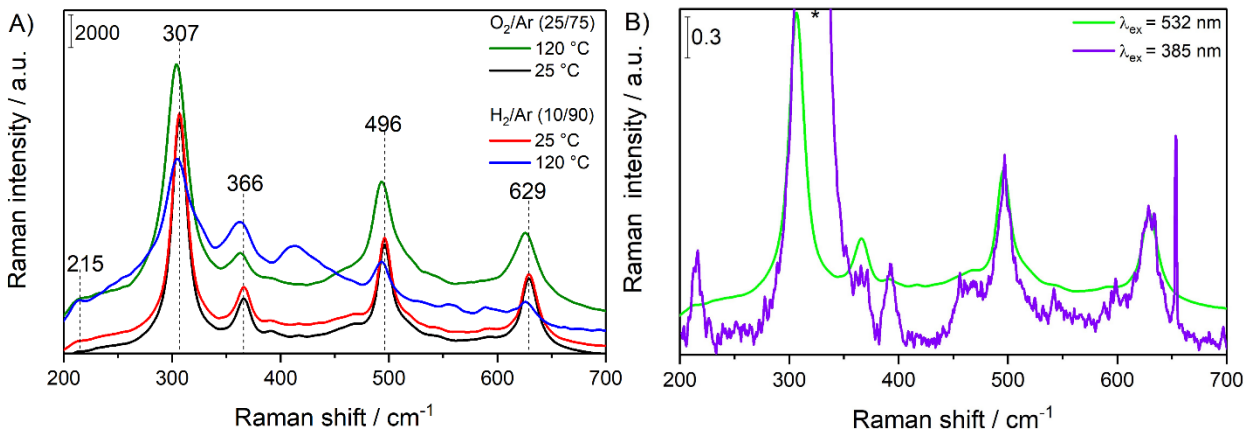

Figure 1: A) *In situ* Raman spectra (λ_{ex} = 532 nm) of In_2O_3 nanoparticles. Spectra were recorded at the indicated temperatures, at a total flow rate of 100 mL/min, and by applying a feed of 25 % O_2/Ar for oxidative and of 10 % H_2/Ar for reductive conditions. **B)** Comparison of two *in situ* Raman spectra, at 532 nm (green) and 385 nm (violet) excitation. Both spectra were recorded at 25 °C after pretreatment in O_2/Ar at 120 °C for 1 h. For better comparability, both spectra were normalized to the band at 629 cm^{-1}. The asterisk (*) marks a band originating from the CaF_2 window (λ_{ex} = 385 nm), while the sharp feature at 650 cm^{-1} results from cosmic rays.

In order to understand the nature of these bands, we employed DFT to calculate Raman spectra (for details see SI). Figure 2A shows a comparison of a calculated Raman spectrum of a primitive In_2O_3 cell with an experimental spectrum (385 nm) recorded in O_2/Ar at 25 °C. The theoretical spectrum was scaled to the band at 629 cm^{-1} (factor 1.09). It is noticeable that the theoretical band positions are in excellent agreement with experiment. Furthermore, the Raman spectrum of the unit cell shows the same positions as that of the primitive cell for symmetry reasons (see Figure S11). In addition to the bands detected at 532 nm excitation, new features appear at 392, 467, 542, and 599 cm^{-1}, which can be assigned to vibrations with F_{2g}/E_g (392 cm^{-1}), F_{2g} (467 cm^{-1}), F_{2g} (542 cm^{-1}), and E_g (599 cm^{-1}) symmetry, based on our DFT results and in accordance with the literature.[14]

Summarizing, the above results show that Raman spectra of In_2O_3 can be fully described by DFT. Since a combined experimental and theoretical approach may thus be expected to facilitate the understanding of more complex systems, it was applied to bulk oxygen vacancies in defective In_2O_3. The defect formation in bulk In_2O_3 corresponds to 3.58 eV in the primitive cell and 3.40 eV in the unit cell, which can be attributed to a 50% lower defect concentration in the unit cell, in agreement with the literature.[28–30] In the following, only the primitive cell will be discussed. In this case, our DFT calculations show that the oxygen defect formation energy and the Raman active modes do not differ between the removed oxygen atoms, since all oxygen

atoms are equal and possess C_1 symmetry. Thus, no particular oxygen defect is preferred in bulk In_2O_3.

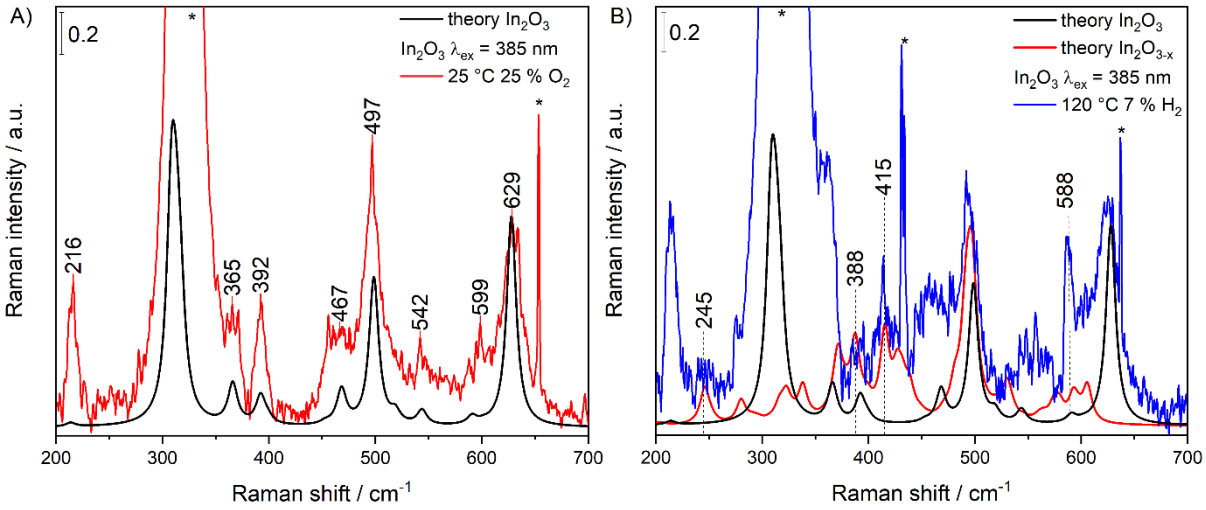

Figure 2: A) Theoretical (DFT) Raman spectrum of a non-defective primitive In_2O_3 ($Ia\bar{3}$) cell (black) compared to the *in situ* 385 nm Raman spectrum (red) of In_2O_3 recorded at 25 °C in 25% O_2/He (pretreatment: 1 h, 120 °C, 25% O_2/He, 50 mL/min). **B)** Theoretical (DFT) Raman spectrum of a defective primitive In_2O_{3-x} ($Ia\bar{3}$) cell (red) compared to the *in situ* 385 nm Raman spectrum (blue) of In_2O_3 recorded at 120 °C in 7% H_2/He (for more details see SI). The total flow rate was always 50 mL/min. The asterisks (*) mark bands originating from the CaF_2 window, while the sharp feature at around 430 cm^{-1} and 650 cm^{-1} results from cosmic rays. For better comparability, all spectra except the theoretical In_2O_{3-x} spectrum are normalized to the 628 cm^{-1} band. The theoretical In_2O_{3-x} spectrum was normalized and scaled (factor: 1.05) to the band at 495 cm^{-1}.

Figure 2B shows a theoretically calculated Raman spectrum of a defective primitive cell (In_2O_{3-x}; red), which is compared with a non-defective cell (black), and an experimental Raman spectrum (λ_{ex} = 385 nm; blue), which was recorded in hydrogen at 120 °C. Again, the theoretical spectrum is in good agreement with the experimental results. In fact, it can be clearly seen by comparison of the two theoretical spectra that the Raman features at 245 cm^{-1}, at around 400 cm^{-1}, and at 588 cm^{-1} are defect-related. To this end, a direct comparison of the

experimental spectra of In_2O_3 and reduced In_2O_3 is shown in Figure S9 for clarity. In addition, theory also shows that the spectrum of In_2O_{3-x} is dominated by accumulations of closely spaced bands. As a consequence, an exact assignment of the symmetry of the individual bands is difficult and of no use experimentally, since the symmetry is lost due to the presence of the defect in the crystal lattice. Hence the detected bands are composed of several non-degenerate vibrations with similar energy, which explains their width, as illustrated for the broad band at around 413 cm^{-1} (see Figure 1A). This feature can be better resolved at 385 nm excitation due to resonance effects, as shown in Figure 2B. The experimental band shape agrees well with that obtained by DFT calculations. According to theory, its width originates from more than ten non-degenerate vibrations with similar symmetry (mostly $\delta(InO_5)$ character). In summary, unlike defect-free In_2O_3, no degeneracy occurs in defect-rich In_2O_3.

A comparison of the two experimental Raman spectra in Figure 2 reveals that in reduced indium oxide the band at 392 cm^{-1} loses its intensity, new bands appear in the region around 400 cm^{-1}, the band at around 550 cm^{-1} loses its asymmetry and becomes wider, and the band at 587 cm^{-1} is more intense. The observed vibrational signature of reduced indium oxide is fully consistent with the simultaneous presence of In_2O_3 and In_2O_{3-x}, based on the combination of the corresponding theoretical spectra (see black and red spectra in Figure 2B). Therefore, hydrogen treatment at 120 °C does not lead to complete reduction. Similar to reduced In_2O_3, the oxygen-treated In_2O_3 shows a feature at 245 cm^{-1} (see Figures 2A and B), which originates from a $\delta(InO_5)$ vibration of In_2O_{3-x} (see Figure 2B), revealing that the oxygen-pretreated In_2O_3 contains oxygen defects.

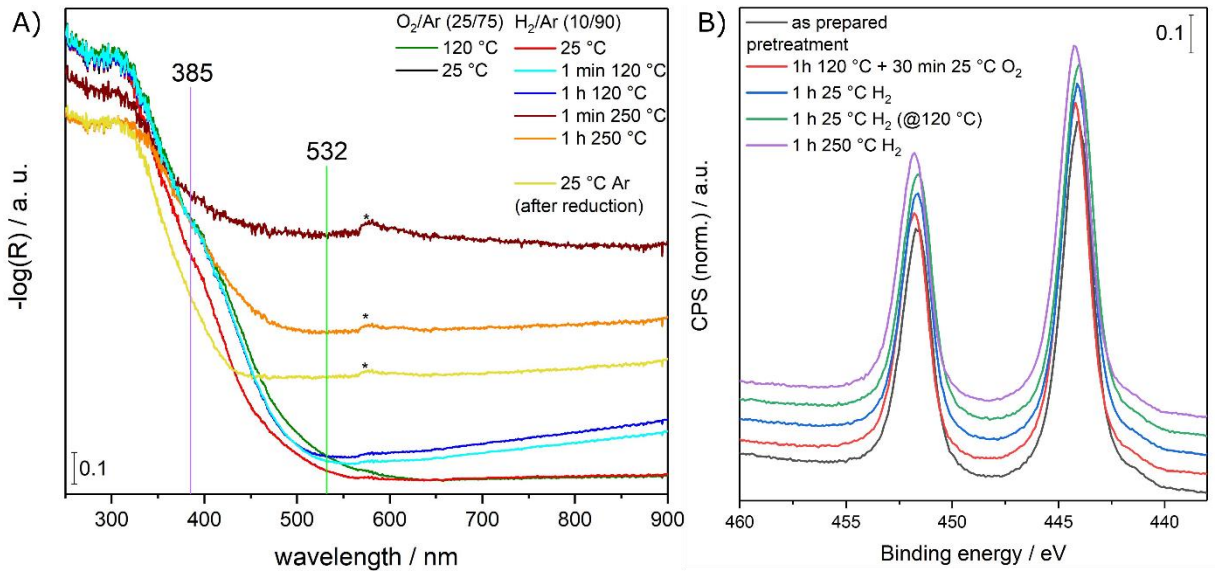

Figure 3: A) *In situ* UV/Vis spectra of In_2O_3 nanoparticles. Spectra were recorded at the indicated temperatures, at a total flow rate of 100 mL/min, and by applying a feed of 25 % O_2/Ar for oxidative and 10 % H_2/Ar for reductive conditions. After reduction at 250 °C, the sample was cooled down to 25 °C in Ar (yellow). Spectra were recorded after about 1 h of equilibration. In addition, for H_2/Ar flow at higher temperatures (>25 °C), spectra are shown after 1 min of equilibration. The asterisks (*) mark a measurement artifact of the spectrometer. Please note that the spectra under O_2 and H_2 at 25 °C overlap. Note that no changes between the spectra at 25 °C in O_2 (black) and H_2 (red) occur. **B)** In 3d photoemission of In_2O_3 nanoparticles. Spectra were normalized to the In $3d_{5/2}$ signal. Spectra were recorded directly after synthesis (black), after O_2 (25%) pretreatment (red), after H_2 (10%) pretreatment at 25 °C (blue, green), and after H_2 pretreatment at 250 °C (violet). All spectra were recorded at 25 °C except the green one, which was recorded at 120 °C. Spectra in B) are offset for clarity.

At 250°C in H_2/Ar flow, acceptable Raman spectra were not accessible at either excitation wavelength. Therefore, we recorded a spectrum at 25 °C in helium after treatment at 250 °C in H_2 flow (see Figure S9), which shows that the defect-related bands become more intense. The aspects that are responsible for the difficult accessibility of the spectra at 250 °C and H_2 will now be considered in more detail, since in contrast to 532 nm, at 385 nm only small changes in the absorption and hence the electronic structure of the particles were detected (see Figure 3A). The observed Raman behavior must therefore be related to other effects. In this

context, XRD measurements (see Figure S2) show that during reduction with hydrogen at 250 °C metallic indium (particle size: 67 nm) is formed and that the particle size of the In_2O_3 particles increases from 19 nm to 29 nm. To understand this behavior in more detail, we explored the changes in the electronic structure and the properties of the surface and bulk by using XP and UV-Vis spectroscopy. Please note that by means of XPS, only surface properties are detected. In contrast, all other methods used in this study probe properties of the whole particle, based on the penetration depth and the size of the particles, which will be referred to as bulk in the following.

Figure 3A depicts *in situ* UV-Vis spectra of indium oxide, which were recorded analogously to the Raman spectra in Figure 1. These spectra clearly show that the sample undergoes significant changes during reduction and oxidation. First, it is noticeable that all spectra are characterized by strong absorption in the UV range, originating from directly allowed transitions into O 2p valence bands.[31,32] In O_2 atmosphere, the absorption between 250 and 450 nm is observed to increase and broaden at 120 °C compared to 25 °C. This behavior is related to an increase of the band gap with rising temperature, as a result of the increased carrier density caused by the Burstein–Moss effect.[33,34] Upon exposure to hydrogen at 25 °C, no changes are detected, consistent with the 532 nm Raman spectra (see Figure 1A). Subsequent heating to 120 °C leads again to a broadening of the absorption within 250–450 nm, indicative of a band-gap increase. In contrast to the spectrum recorded in oxygen (120 °C), the absorption is somewhat lower, suggesting a slightly lower band gap. This behavior can be explained by the formation of defects, which can act as donors, thus creating new energy levels in the near-band-gap region.[35] Furthermore, Figure 3A shows an increase in absorption in the visible range (>500 nm). In contrast to lower temperatures (<120 °C), the absorption continues to grow after 1 h of treatment. Upon switching to 250 °C, it reaches a maximum after 1 min and decreases during the following 59 min. The origin of these changes in Vis absorption can be explained by the presence of defects located at or near the surface.[35] Besides, at 250 °C in hydrogen, the

formation of metallic indium is conceivable, as evidenced by XRD measurements after treatment (see Figure S2). However, the absorption of indium surface plasmons is not as broad as the defect-induced absorption.[36,37] We therefore attribute the observed changes in absorption to a combination of the two effects.

The time-dependent dynamics can be explained by a balance between bulk oxygen and surface vacancies. As a consequence, at a high concentration of surface defects a transfer of oxygen from the bulk to the surface takes place until an equilibrium state is reached. Such a scenario is supported by quasi *in situ* XPS measurements (for details see SI), which show that, despite indium oxide reduction, the oxygen concentration on the surface slightly increases (see O:In ratios in Table S1). Thus, starting at 120 °C there is an exchange of oxygen between the bulk and defects at the surface. This can also be demonstrated by heating the sample to 120 °C in the XPS analysis chamber after the same H_2 pretreatment at 25 °C as mentioned before (see Figure 1A), while simultaneously recording mass spectra showing the release of CO_2 and H_2O. The XP spectrum recorded at 120 °C reveals an increase in the surface O:In ratio compared to 25 °C, despite desorption of CO_2 and H_2O (see Table S1).

Returning to the XRD results, which showed formation of metallic indium, we performed XPS measurements of the sample after the same pretreatment (250 °C, 10% H_2). These spectra show a higher amount of oxygen than during reduction at lower temperatures. On the other hand, there is no evidence of metallic indium or indium in oxidation states other than In^{3+} (see Figure 3B). This clearly demonstrates that at higher temperatures (>120 °C) oxygen is transported from the bulk to the surface. Thus despite the lower defect energy on the surface,[38] defects in the bulk seem to be preferred. In this context, it has previously been shown that oxygen vacancies are the predominant donor in In_2O_3 and are responsible for the oxygen self-diffusion process.[39] These results are also underlined by theoretical studies which propose that oxygen vacancies are already mobile at temperatures of about 400 K.[40]

Summarizing, in this study we elucidated the oxygen dynamics of oxidized and reduced cubic In_2O_3 nanoparticles by a combination of spectroscopic techniques supported by theoretical calculations. We have shown that surface oxygen defects are in equilibrium with the bulk at temperatures above 120 °C and that in the equilibrium state bulk defects are preferred over surface defects, resulting in a lower defect formation on the surface. We furthermore demonstrated that experimental vibrational Raman spectra of In_2O_3 and In_2O_{3-x} are in excellent agreement with those calculated by DFT. By exploiting resonance effects, for example at 385 nm excitation, and facilitated by theoretical calculations, new insight into the nature of vibrational bands was provided, such as the band at 245 cm^{-1}, which was assigned to a $\delta(InO_5)$ vibration in defective In_2O_3. Finally, while our findings highlight the potential of combining multiple *in situ* spectroscopic and theoretical analysis to unravel the redox dynamics of cubic In_2O_3, such an approach may be of great interest for other reducible oxide materials as well for their structural characterization under catalytic conditions.

Acknowledgements

The DFT calculations were conducted using the Lichtenberg high performance computer of the TU Darmstadt. We thank Stefan Lauterbach and Hans-Joachim Kleebe for TEM measurements, Martin Brodrecht for nitrogen adsorption/desorption experiments, Kathrin Hofmann for XRD analysis, M. Verónica Ganduglia Pirovano for helpful discussions, and Karl Kopp for technical support.

Supporting Information

Detailed information on experimental and theoretical methods as well as additional experimental data.

References

(1) Sun, Q.; Ye, J.; Liu, C.; Ge, Q. In_2O_3 as a Promising Catalyst for CO_2 Utilization: A Case Study with Reverse Water Gas Shift over In_2O_3. *Greenh. Gases Sci. Technol.* **2014**, *4* (1), 140–144. https://doi.org/10.1002/ghg.1401.

(2) Wang, J.; Liu, C.-Y.; Senftle, T. P.; Zhu, J.; Zhang, G.; Guo, X.; Song, C. Variation in the In_2O_3 Crystal Phase Alters Catalytic Performance toward the Reverse Water Gas Shift Reaction. *ACS Catal.* **2020**, *10* (5), 3264–3273. https://doi.org/10.1021/acscatal.9b04239.

(3) Wang, W.; Zhang, Y.; Wang, Z.; Yan, J.; Ge, Q.; Liu, C. Reverse Water Gas Shift over In_2O_3 – CeO_2 Catalysts. *Catal. Today* **2016**, *259* (Part 2), 402–408. https://doi.org/10.1016/j.cattod.2015.04.032.

(4) Tsoukalou, A.; Abdala, P. M.; Stoian, D.; Huang, X.; Willinger, M. G.; Fedorov, A.; Müller, C. R. Structural Evolution and Dynamics of an In_2O_3 Catalyst for CO_2 Hydrogenation to Methanol: An Operando XAS-XRD and in Situ TEM Study. *J. Am. Chem. Soc.* **2019**, *141* (34), 13497–13505. https://doi.org/10.1021/jacs.9b04873.

(5) Frei, M. S.; Capdevila-Cortada, M.; García-Muelas, R.; Mondelli, C.; López, N.; Stewart, J. A.; Curulla Ferré, D.; Pérez-Ramírez, J. Mechanism and Microkinetics of Methanol Synthesis via CO_2 Hydrogenation on Indium Oxide. *J. Catal.* **2018**, *361* (1), 313–321. https://doi.org/10.1016/j.jcat.2018.03.014.

(6) Ye, J.; Liu, C.; Mei, D.; Ge, Q. Active Oxygen Vacancy Site for Methanol Synthesis from CO_2 Hydrogenation on In_2O_3(110): A DFT Study. *ACS Catal.* **2013**, *3* (6), 1296–1306. https://doi.org/10.1021/cs400132a.

(7) Wang, J.; Zhang, G.; Zhu, J.; Zhang, X.; Ding, F.; Zhang, A.; Guo, X.; Song, C. CO_2 Hydrogenation to Methanol over In_2O_3 - Based Catalysts: From Mechanism to Catalyst Development. *ACS Catal.* **2021**, *11* (3), 1406–1423. https://doi.org/10.1021/acscatal.0c03665.

(8) Qin, B.; Li, S. First Principles Investigation of Dissociative Adsorption of H_2 during CO_2 Hydrogenation over Cubic and Hexagonal In_2O_3 Catalysts. *Phys. Chem. Chem. Phys.* **2020**, *22*, 3390–3399. https://doi.org/10.1039/C9CP05867B.

(9) Rui, N.; Zhang, F.; Sun, K.; Liu, Z.; Xu, W.; Stavitski, E.; Senanayake, S. D.; Rodriguez, J. A.; Liu, C.-J. Hydrogenation of CO_2 to Methanol on a $Au^{\delta+}$–In_2O_{3-x} Catalyst. *ACS Catal.* **2020**, *10* (19), 11307–11317. https://doi.org/10.1021/acscatal.0c02120.

(10) Yan, H.; He, K.; Samek, I. A.; Jing, D.; Nanda, M. G.; Stair, P. C.; Notestein, J. M. Tandem In_2O_3-Pt/Al_2O_3 Catalyst for Coupling of Propane Dehydrogenation to Selective H_2 Combustion. *Science.* **2021**, *371* (6535), 1257–1260. https://doi.org/10.1126/science.abd4441.

(11) Bielz, T.; Lorenz, H.; Jochum, W.; Kaindl, R.; Klauser, F.; Klötzer, B.; Penner, S. Hydrogen on In_2O_3: Reducibility, Bonding, Defect Formation, and Reactivity. *J. Phys. Chem. C* **2010**, *114* (19), 9022–9029. https://doi.org/10.1021/jp1017423.

(12) Gervasini, A.; Perdigon-Melon, J. A.; Guimon, C.; Auroux, A. An In-Depth Study of Supported In_2O_3 Catalysts for the Selective Catalytic Reduction of NO_x: The Influence of the Oxide Support. *J. Phys. Chem. B* **2006**, *110* (1), 240–249. https://doi.org/10.1021/jp0532824.

(13) Garcia-Domene, B.; Ortiz, H. M.; Gomis, O.; Sans, J. A.; Manjón, F. J.; Muñoz, A.; Rodríguez-Hernández, P.; Achary, S. N.; Errandonea, D.; Martínez-García, D.; Romero, A. H.; Singhal, A.; Tyagi, A. K. High-Pressure Lattice Dynamical Study of Bulk and Nanocrystalline In_2O_3. *J. Appl. Phys.* **2012**, *112* (12), 123511. https://doi.org/10.1063/1.4769747.

(14) Kranert, C.; Schmidt-Grund, R.; Grundmann, M. Raman Active Phonon Modes of Cubic In_2O_3. *Phys. status solidi - Rapid Res. Lett.* **2014**, *8* (6), 554–559.

https://doi.org/10.1002/pssr.201409004.

(15) Berengue, O. M.; Rodrigues, A. D.; Dalmaschio, C. J.; Lanfredi, A. J. C.; Leite, E. R.; Chiquito, A. J. Structural Characterization of Indium Oxide Nanostructures: A Raman Analysis. *J. Phys. D. Appl. Phys.* **2010**, *43* (4), 045401. https://doi.org/10.1088/0022-3727/43/4/045401.

(16) Wang, C. Y.; Dai, Y.; Pezoldt, J.; Lu, B.; Kups, T.; Cimalla, V.; Ambacher, O. Phase Stabilization and Phonon Properties of Single Crystalline Rhombohedral Indium Oxide. *Cryst. Growth Des.* **2008**, *8* (4), 1257–1260. https://doi.org/10.1021/cg700910n.

(17) Panneerdoss, I. J.; Jeyakumar, S. J.; Ramalingam, S.; Jothibas, M. Characterization of Prepared In_2O_3 Thin Films: The FT-IR, FT-Raman, UV–Visible Investigation and Optical Analysis. *Spectrochim. Acta Part A Mol. Biomol. Spectrosc.* **2015**, *147*, 1–13. https://doi.org/10.1016/j.saa.2015.02.033.

(18) Ramsteiner, M.; Feldl, J.; Galazka, Z. Signatures of Free Carriers in Raman Spectra of Cubic In_2O_3. *Semicond. Sci. Technol.* **2020**, *35* (1), 015017. https://doi.org/10.1088/1361-6641/ab5615.

(19) Gan, J.; Lu, X.; Wu, J.; Xie, S.; Zhai, T.; Yu, M.; Zhang, Z.; Mao, Y.; Wang, S. C. I.; Shen, Y.; Tong, Y. Oxygen Vacancies Promoting Photoelectrochemical Performance of In_2O_3 Nanocubes. *Sci. Rep.* **2013**, *3* (1), 1021. https://doi.org/10.1038/srep01021.

(20) Wang, X.; Zhang, M.; Liu, J.; Luo, T.; Qian, Y. Shape- and Phase-Controlled Synthesis of In_2O_3 with Various Morphologies and Their Gas-Sensing Properties. *Sensors Actuators B Chem.* **2009**, *137* (1), 103–110. https://doi.org/10.1016/j.snb.2008.11.027.

(21) Sun, Y.; Murphy, C. J.; Reyes-Gil, K. R.; Reyes-Garcia, E. A.; Lilly, J. P.; Raftery, D. Carbon-Doped In_2O_3 Films for Photoelectrochemical Hydrogen Production. *Int. J. Hydrogen Energy* **2008**, *33* (21), 5967–5974. https://doi.org/10.1016/j.ijhydene.2008.07.100.

(22) Elouali, S.; Bloor, L. G.; Binions, R.; Parkin, I. P.; Carmalt, C. J.; Darr, J. A. Gas

Sensing with Nano-Indium Oxides (In_2O_3) Prepared via Continuous Hydrothermal Flow Synthesis. *Langmuir* **2012**, *28* (3), 1879–1885. https://doi.org/10.1021/la203565h.

(23) Andrews, L.; Wang, X. Infrared Spectra of Indium Hydrides in Solid Hydrogen and of Solid Indane. *Angew. Chemie* **2004**, *116* (13), 1738–1741. https://doi.org/10.1002/ange.200353216.

(24) Wang, X.; Andrews, L. Infrared Spectra of Indium Hydrides in Solid Hydrogen and Neon. *J. Phys. Chem. A* **2004**, *108* (20), 4440–4448. https://doi.org/10.1021/jp037942l.

(25) Fontcuberta i Morral, A.; Zahler, J. M.; Griggs, M. J.; Atwater, H. A.; Chabal, Y. J. Spectroscopic Studies of the Mechanism for Hydrogen-Induced Exfoliation of InP. *Phys. Rev. B* **2005**, *72* (8), 085219. https://doi.org/10.1103/PhysRevB.72.085219.

(26) Liu, N.; Kuech, T. F. Interfacial Chemistry of InP/GaAs Bonded Pairs. *J. Electron. Mater.* **2007**, *36* (3), 179–190. https://doi.org/10.1007/s11664-006-0077-1.

(27) Maeno, Z.; Yasumura, S.; Wu, X.; Huang, M.; Liu, C.; Toyao, T.; Shimizu, K. Isolated Indium Hydrides in CHA Zeolites: Speciation and Catalysis for Nonoxidative Dehydrogenation of Ethane. *J. Am. Chem. Soc.* **2020**, *142* (10), 4820–4832. https://doi.org/10.1021/jacs.9b13865.

(28) Walsh, A.; Catlow, C. R. A.; Sokol, A. A.; Woodley, S. M. Physical Properties, Intrinsic Defects, and Phase Stability of Indium Sesquioxide. *Chem. Mater.* **2009**, *21* (20), 4962–4969. https://doi.org/10.1021/cm902280z.

(29) Walsh, A.; Sokol, A. A.; Catlow, C. R. A. Free Energy of Defect Formation: Thermodynamics of Anion Frenkel Pairs in Indium Oxide. *Phys. Rev. B* **2011**, *83* (22), 224105. https://doi.org/10.1103/PhysRevB.83.224105.

(30) Ágoston, P.; Erhart, P.; Klein, A.; Albe, K. Geometry, Electronic Structure and Thermodynamic Stability of Intrinsic Point Defects in Indium Oxide. *J. Phys. Condens. Matter* **2009**, *21* (45). https://doi.org/10.1088/0953-8984/21/45/455801.

(31) Novkovski, N.; Tanuševski, A. Origin of the Optical Absorption of In_2O_3 Thin Films in the Visible Range. *Semicond. Sci. Technol.* **2008**, *23* (9), 095012. https://doi.org/10.1088/0268-1242/23/9/095012.

(32) Schleife, A.; Neumann, M. D.; Esser, N.; Galazka, Z.; Gottwald, A.; Nixdorf, J.; Goldhahn, R.; Feneberg, M. Optical Properties of In_2O_3 from Experiment and First-Principles Theory: Influence of Lattice Screening. *New J. Phys.* **2018**, *20* (5), 053016. https://doi.org/10.1088/1367-2630/aabeb0.

(33) Burstein, E. Anomalous Optical Absorption Limit in InSb. *Phys. Rev.* **1954**, *93* (3), 632–633. https://doi.org/10.1103/PhysRev.93.632.

(34) Moss, T. S. The Interpretation of the Properties of Indium Antimonide. *Proc. Phys. Soc. Sect. B* **1954**, *67* (10), 775–782. https://doi.org/10.1088/0370-1301/67/10/306.

(35) Gu, F.; Li, C.; Han, D.; Wang, Z. Manipulating the Defect Structure (V_O) of In_2O_3 Nanoparticles for Enhancement of Formaldehyde Detection. *ACS Appl. Mater. Interfaces* **2018**, *10* (1), 933–942. https://doi.org/10.1021/acsami.7b16832.

(36) Cingarapu, S.; Yang, Z.; Sorensen, C. M.; Klabunde, K. J. Synthesis of Indium Nanoparticles: Digestive Ripening under Mild Conditions. *Inorg. Chem.* **2011**, *50* (11), 5000–5005. https://doi.org/10.1021/ic200232b.

(37) Khanna, P. K.; Jun, K.-W.; Hong, K. B.; Baeg, J.-O.; Chikate, R. C.; Das, B. K. Colloidal Synthesis of Indium Nanoparticles by Sodium Reduction Method. *Mater. Lett.* **2005**, *59* (8–9), 1032–1036. https://doi.org/10.1016/j.matlet.2004.11.050.

(38) Walsh, A. Surface Oxygen Vacancy Origin of Electron Accumulation in Indium Oxide. *Appl. Phys. Lett.* **2011**, *98* (26), 261910. https://doi.org/10.1063/1.3604811.

(39) Tang, A.; Mei, Z.; Huo, W.; Du, X. Self-Diffusion Measurements in In_2O_3 Isotopic Heterostructures: Oxygen Vacancy Energetics. *Sci. China Physics, Mech. Astron.* **2018**, *61* (11), 117321. https://doi.org/10.1007/s11433-018-9209-9.

(40) Ágoston, P.; Albe, K. Ab Initio Modeling of Diffusion in Indium Oxide. *Phys. Rev. B*

2010, *81* (19), 195205. https://doi.org/10.1103/PhysRevB.81.195205.